Eleventh International Conference on Computational Fluid Dynamics (ICCFD11), Maui, Hawaii, July 11-15, 2022

ICCFD11-2022-0404

Obtaining Accurate Functionals from High-Order Generalized Summation-by-Parts Discretizations in Curvilinear Coordinates

D.A. Craig Penner and D.W. Zingg
Corresponding author: david.craigpenner@mail.utoronto.ca

University of Toronto Institute for Aerospace Studies, Canada.

Abstract: Results are presented that summarize how to obtain accurate functionals from dual-consistent generalized summation-by-parts discretizations when solving problems of increasing practical complexity. These results include showing that an optimized approach for approximating grid metrics is important for obtaining accurate functionals with Legendre-Gauss operators, showing that the mortar-element approach outperforms the global summation-by-parts-operator approach with respect to functional accuracy in certain situations, and showing that the use of degree $p+1$ geometry representations in the presence of flow tangency boundary conditions is beneficial for functional accuracy.

Keywords: High-Order Methods, Functional Superconvergence, Generalized Summation-by-Parts, Curvilinear Coordinates.

1 Introduction

In computational aerodynamics, the primary quantities of interest are often directly related to integral functionals like lift and drag. The theory of functional superconvergence dictates that a degree p dual-consistent discretization can lead to at least $2p$-order-accurate functionals when the solution is sufficiently smooth [8], which is desirable in the context of optimization problems in computational aerodynamics [10]. It is known that classical summation-by-parts (CSBP) schemes can lead to superconvergent functionals [11, 12]. Recently, a more general class of summation-by-parts (SBP) schemes has been introduced that are referred to as generalized SBP schemes [6]. There are indications that some generalized SBP schemes lead to superconvergent functionals [7, 19, 18]; however, for some schemes suboptimal functional convergence is observed [3].

The objective of this paper is to synthesize recent work on generalized SBP schemes detailing how to obtain accurate functionals from generalized SBP discretizations of hyperbolic partial differential equations (PDEs) of increasing practical relevance. Beginning in one dimension, it is shown that accurate functionals can be obtained from generalized SBP discretizations of a scalar linear boundary-value problem under certain conditions. Next, results in two dimensions based on the mortar-element and global SBP-operator approaches are presented. Finally, the extension to the Euler equations is summarized.

2 Overview of Discretizations

In this paper, generalized SBP discretizations of one- and two-dimensional scalar boundary-value problems and the Euler equations in two dimensions are considered. Only steady problems are considered; however, all ideas covered extend directly to unsteady problems. Details regarding the one-dimensional discretization may be found in [3]. For the two-dimensional boundary-value problem, mortar-element and global SBP-operator discretizations (see [5] for details) of divergence and skew-symmetric forms of the governing equation are

considered. For the Euler equations, based on results from studies with the boundary-value problem, a mortar-element discretization of the divergence form of the governing equations is considered. More details regarding the two-dimensional discretizations may be found in [2].

2.1 Mortar-Element and Global SBP-Operator Approaches

To develop a general understanding of the mortar-element and global SBP-operator approaches (as first introduced in [5]), it is instructive to consider an example based on the following two-dimensional boundary-value problem:

$$\begin{aligned} \nabla \cdot \boldsymbol{\mathcal{F}} \coloneqq \sum_{m=1}^{2} \frac{\partial (a_m \mathcal{U})}{\partial x_m} = \mathcal{S} \quad &\text{in } \Omega, \\ \mathcal{U} = \mathcal{U}^- \quad &\text{on } \Gamma^-, \end{aligned} \tag{1}$$

where $\mathcal{U}$ is the solution, $\mathcal{S}$ is the source term, and a_m are constants. The boundary Γ^- is defined by $\Gamma^- \coloneqq \{(x_1, x_2) \in \Gamma \mid \boldsymbol{a} \cdot \boldsymbol{n} \leq 0\}$, where $\boldsymbol{a} = [a_1, a_2]^{\mathrm{T}}$ and $\boldsymbol{n}$ is the outward unit normal vector. The boundary Γ^+ is defined by $\Gamma^+ \coloneqq \Gamma \setminus \Gamma^-$. On a single element, the transformed skew-symmetric form of (1) is given by

$$\begin{gathered} \frac{1}{2} \left\{ \nabla \cdot \boldsymbol{\mathcal{F}} + \Lambda \cdot \nabla \mathcal{U} \right\} \coloneqq \\ \frac{1}{2} \sum_{l=1}^{2} \left\{ \frac{\partial}{\partial \xi_l} \left(\sum_{m=1}^{2} \mathcal{J} \frac{\partial \xi_l}{\partial x_m} \mathcal{U} \right) + \sum_{m=1}^{2} \mathcal{J} \frac{\partial \xi_l}{\partial x_m} \frac{\partial \mathcal{U}}{\partial \xi_l} \right\} = \mathcal{J} \mathcal{S} \quad \text{in } \hat{\Omega}, \end{gathered} \tag{2}$$

where

$$\Lambda \coloneqq \left[\sum_{m=1}^{2} \mathcal{J} \frac{\partial \xi_1}{\partial x_m}, \sum_{m=1}^{2} \mathcal{J} \frac{\partial \xi_2}{\partial x_m} \right]^{\mathrm{T}}$$

and $\mathcal{J}$ is the Jacobian of the transformation from physical coordinates to computational coordinates, $\mathcal{T} \colon \hat{\Omega} \to \Omega$. See, for example, [16] for the definition of the Jacobian and the various metric terms in two dimensions. Furthermore, for simplicity, it is assumed that $\boldsymbol{a} = [1, 1]^{\mathrm{T}}$ for the present example, but $a_m \neq 1$ is introduced for the numerical examples.

Suppose one wishes to discretize the skew-symmetric form of the two-dimensional boundary-value problem using two elements that share an interface perpendicular to the ξ_1 direction (face 2 on the left element and face 1 on the right element), as depicted in Figure 1. For the mortar-element approach, the surface quadrature nodes are defined on mortar faces that are introduced at element interfaces and boundaries and the grid metrics are defined on the mortar faces. In contrast, for the global SBP-operator approach, a global SBP operator is constructed over the entire grid, no mortar faces are introduced, and the grid metrics are approximated using the global SBP operators. In this paper, $\mathsf{D}_{\xi_l}^{(1\mathrm{D})}$ denotes a one-dimensional generalized SBP matrix operator approximating the first derivative in the direction ξ_l, and is associated with the symmetric and positive-definite one-dimensional norm matrix $\mathsf{H}_{\xi_l}^{(1\mathrm{D})}$. In two-dimensions, the various operators are constructed via Kronecker tensor products. For example, in the direction ξ_1,

$$\begin{aligned} &\mathsf{H} \coloneqq \mathsf{H}_{\xi_1}^{(1\mathrm{D})} \otimes \mathsf{H}_{\xi_2}^{(1\mathrm{D})} \otimes \mathsf{I}_m, \\ &\mathsf{D}_{\xi_1} \coloneqq \mathsf{H}^{-1} \mathsf{Q}_{\xi_1}, && \mathsf{Q}_{\xi_1} \coloneqq \mathsf{Q}_{\xi_1}^{(1\mathrm{D})} \otimes \mathsf{H}_{\xi_2}^{(1\mathrm{D})} \otimes \mathsf{I}_m, \\ &\mathsf{E}_{\xi_1} \coloneqq \mathsf{E}_{\beta_{\xi_1}} + \mathsf{E}_{\alpha_{\xi_1}}, && \mathsf{E}_{\beta_{\xi_1}} \coloneqq \mathsf{R}_{\beta_{\xi_1}}^{\mathrm{T}} \mathsf{H}_{\xi_1}^{\perp} \mathsf{R}_{\beta_{\xi_1}}, && \mathsf{E}_{\alpha_{\xi_1}} \coloneqq -\mathsf{R}_{\alpha_{\xi_1}}^{\mathrm{T}} \mathsf{H}_{\xi_1}^{\perp} \mathsf{R}_{\alpha_{\xi_1}}, \\ &\mathsf{H}_{\xi_1}^{\perp} \coloneqq \mathsf{H}_{\xi_2}^{(1\mathrm{D})} \otimes \mathsf{I}_m, && \mathsf{R}_{\beta_{\xi_1}} \coloneqq \boldsymbol{t}_{\beta_{\xi_1}}^{\mathrm{T}} \otimes \mathsf{I}_{\xi_2} \otimes \mathsf{I}_m, && \mathsf{R}_{\alpha_{\xi_1}} \coloneqq \boldsymbol{t}_{\alpha_{\xi_1}}^{\mathrm{T}} \otimes \mathsf{I}_{\xi_2} \otimes \mathsf{I}_m, \end{aligned}$$

where a system of m equations is being discretized and I_m is an identity matrix. The extrapolation operators $\mathsf{R}_{\alpha_{\xi_1}}$ and $\mathsf{R}_{\beta_{\xi_1}}$ approximate the following quantities [5]:

$$\mathsf{R}_{\alpha_{\xi_1}} \boldsymbol{u}_\kappa \approx \mathcal{U}_\kappa(\boldsymbol{\xi}_1^{\alpha_{\xi_1}}, \boldsymbol{\xi}_2^{\alpha_{\xi_1}}) \quad \text{and} \quad \mathsf{R}_{\beta_{\xi_1}} \boldsymbol{u}_\kappa \approx \mathcal{U}_\kappa(\boldsymbol{\xi}_1^{\beta_{\xi_1}}, \boldsymbol{\xi}_2^{\beta_{\xi_1}}),$$

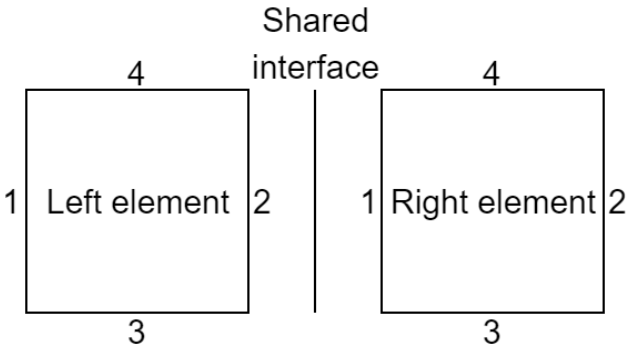

Figure 1: Schematic diagram showing the two-element example. The faces on each element are numbered 1 through 4. The vertical line denoting the shared interface corresponds to face 2 on the left element and face 1 on the right element.

where, for example, $\boldsymbol{\xi}_1^{\alpha_{\xi_1}}$ and $\boldsymbol{\xi}_2^{\alpha_{\xi_1}}$ are the coordinates of the nodes on the surface $\hat{\Gamma}_\kappa^{\alpha_{\xi_1}}$, which is perpendicular to ξ_1. The vectors $\boldsymbol{\xi}_1^{\beta_{\xi_1}}$ and $\boldsymbol{\xi}_2^{\beta_{\xi_1}}$ are defined in a similar manner. Finally, the superscripts L and R denote terms corresponding to the left and right elements, respectively.

For the present two-element example, consider the discretization on the left element using the mortar-element approach, given by

$$\begin{aligned}
&\frac{1}{2}\sum_{l,m=1}^{2}\left\{\mathsf{D}_{\xi_l}\,\mathrm{diag}\left(\mathcal{J}\frac{\partial \xi_l}{\partial x_m}\right)_h^{\mathrm{L}}+\mathrm{diag}\left(\mathcal{J}\frac{\partial \xi_l}{\partial x_m}\right)_h^{\mathrm{L}}\mathsf{D}_{\xi_l}\right\}\boldsymbol{u}_h^{\mathrm{L}}=\mathrm{diag}\left(\mathcal{J}_h\right)^{\mathrm{L}}\boldsymbol{s}^{\mathrm{L}}\\
&+\mathsf{H}^{-1}\left\{-\mathsf{R}_{\alpha_{\xi_1}}^{\mathrm{T}}\mathsf{H}_{\xi_1}^{\perp}\left(\boldsymbol{f}_{(1),h}^{\mathrm{L}}(\boldsymbol{u}_h^{\mathrm{L}})-\boldsymbol{f}_{(1),h}^{\star,\mathrm{L}}(\boldsymbol{u}_h^{\mathrm{L}})\right)\right\}+\mathsf{H}^{-1}\left\{-\mathsf{R}_{\alpha_{\xi_2}}^{\mathrm{T}}\mathsf{H}_{\xi_2}^{\perp}\left(\boldsymbol{f}_{(3),h}^{\mathrm{L}}(\boldsymbol{u}_h^{\mathrm{L}})-\boldsymbol{f}_{(3),h}^{\star,\mathrm{L}}(\boldsymbol{u}_h^{\mathrm{L}})\right)\right\}\\
&+\mathsf{H}^{-1}\left\{\ \mathsf{R}_{\beta_{\xi_1}}^{\mathrm{T}}\mathsf{H}_{\xi_1}^{\perp}\left(\boldsymbol{f}_{(2),h}^{\mathrm{L}}(\boldsymbol{u}_h^{\mathrm{L}})-\boldsymbol{f}_{(2),h}^{\star,\mathrm{L}}(\boldsymbol{u}_h^{\mathrm{L}})\right)\right\}+\mathsf{H}^{-1}\left\{\ \mathsf{R}_{\beta_{\xi_2}}^{\mathrm{T}}\mathsf{H}_{\xi_2}^{\perp}\left(\boldsymbol{f}_{(4),h}^{\mathrm{L}}(\boldsymbol{u}_h^{\mathrm{L}})-\boldsymbol{f}_{(4),h}^{\star,\mathrm{L}}(\boldsymbol{u}_h^{\mathrm{L}})\right)\right\},
\end{aligned}\tag{3}$$

where, for example, the flux in the boundary SAT for face 1 of the left element is given by

$$\boldsymbol{f}_{(1),h}^{\mathrm{L}}(\boldsymbol{u}_h^{\mathrm{L}}) \coloneqq \sum_{m=1}^{2}\mathsf{R}_{\alpha_{\xi_1}}\,\mathrm{diag}\left(\mathcal{J}\frac{\partial \xi_1}{\partial x_m}\right)_h^{\mathrm{L}}\boldsymbol{u}_h^{\mathrm{L}}$$

and the numerical boundary flux function for face 1 of the left element is given by

$$\boldsymbol{f}_{(1),h}^{\star,\mathrm{L}}(\boldsymbol{u}_h^{\mathrm{L}}) \coloneqq \frac{1}{2}\left(\Lambda_{(1),h}^{\mathrm{L}}\boldsymbol{u}_{[1]}^{\mathrm{L}}+\mathsf{R}_{\alpha_{\xi_1}}\sum_{m=1}^{2}\mathrm{diag}\left(\mathcal{J}\frac{\partial \xi_1}{\partial x_m}\right)_h^{\mathrm{L}}\boldsymbol{u}_h^{\mathrm{L}}\right)-\frac{1}{2}\left|\Lambda_{(1),h}^{\mathrm{L}}\right|\left(\mathsf{R}_{\alpha_{\xi_1}}\boldsymbol{u}_h^{\mathrm{L}}-\boldsymbol{u}_{[1]}^{\mathrm{L}}\right).$$

Here, the grid metrics on the mortar faces are defined by

$$\Lambda_{(1),h}^{\mathrm{L}} \coloneqq \sum_{m=1}^{2}\mathrm{diag}\left(\mathcal{J}\frac{\partial \xi_1}{\partial x_m}\right)_h^{[1],\mathrm{L}},$$

for example, and $\boldsymbol{u}_{[1]}^{\mathrm{L}}$, $\boldsymbol{u}_{[3]}^{\mathrm{L}}$, $\boldsymbol{u}_{[4]}^{\mathrm{L}}$, $\boldsymbol{u}_{[2]}^{\mathrm{R}}$, $\boldsymbol{u}_{[3]}^{\mathrm{R}}$, and $\boldsymbol{u}_{[4]}^{\mathrm{R}}$ hold boundary data. Finally, $\boldsymbol{s}^{\mathrm{L}}$ is a restriction of the continuous source term to the nodes of the left element. For the mortar-element discretizations, the baseline or modified approaches for the metrics can be used. For the baseline approach, the volume metric terms are approximated using the same SBP operator used to discretize the flux terms and the surface metric terms are constructed by extrapolating the volume metric terms to the surface of each element. For the modified approach, the volume metrics on element κ are determined by solving a strictly convex quadratic optimization problem [4, 5].

Unlike the mortar-element approach, no mortar faces are introduced for the global SBP-operator approach. Instead, in the context of the present two-element example, the discretization on the left element,

for example, can be constructed directly as

$$
\begin{aligned}
&\frac{1}{2}\sum_{l,m=1}^{2}\left\{\mathsf{D}_{\xi_l}\,\mathrm{diag}\left(\mathcal{J}\frac{\partial \xi_l}{\partial x_m}\right)_h^{\mathrm{L}}+\mathrm{diag}\left(\mathcal{J}\frac{\partial \xi_l}{\partial x_m}\right)_h^{\mathrm{L}}\mathsf{D}_{\xi_l}\right\}\boldsymbol{u}_h^{\mathrm{L}}=\mathrm{diag}\left(\mathcal{J}_h\right)^{\mathrm{L}}\boldsymbol{s}^{\mathrm{L}}\\
&-\frac{1}{2}\mathsf{H}^{-1}\left\{\frac{1}{2}\mathsf{R}_{\alpha_{\xi_1}}^{\mathrm{T}}\mathsf{H}_{\xi_1}^{\perp}\mathsf{R}_{\alpha_{\xi_1}}\left(\Lambda_{h,1}^{\mathrm{L}}+\left|\Lambda_{h,1}^{\mathrm{L}}\right|\right)+\frac{1}{2}\left(\Lambda_{h,1}^{\mathrm{L}}+\left|\Lambda_{h,1}^{\mathrm{L}}\right|\right)\mathsf{R}_{\alpha_{\xi_1}}^{\mathrm{T}}\mathsf{H}_{\xi_1}^{\perp}\mathsf{R}_{\alpha_{\xi_1}}\right\}\left(\boldsymbol{u}_h^{\mathrm{L}}-\tilde{\mathsf{I}}_{\xi_1}\boldsymbol{u}_{[1]}^{\mathrm{L}}\right)\\
&+\frac{1}{2}\mathsf{H}^{-1}\left\{\frac{1}{2}\mathsf{R}_{\beta_{\xi_1}}^{\mathrm{T}}\mathsf{H}_{\xi_1}^{\perp}\mathsf{R}_{\beta_{\xi_1}}\left(\Lambda_{h,1}^{\mathrm{L}}-\left|\Lambda_{h,1}^{\mathrm{L}}\right|\right)+\frac{1}{2}\left(\Lambda_{h,1}^{\mathrm{L}}-\left|\Lambda_{h,1}^{\mathrm{L}}\right|\right)\mathsf{R}_{\beta_{\xi_1}}^{\mathrm{T}}\mathsf{H}_{\xi_1}^{\perp}\mathsf{R}_{\beta_{\xi_1}}\right\}\boldsymbol{u}_h^{\mathrm{L}}\\
&-\frac{1}{2}\mathsf{H}^{-1}\left\{\frac{1}{2}\mathsf{R}_{\beta_{\xi_1}}^{\mathrm{T}}\mathsf{H}_{\xi_1}^{\perp}\mathsf{R}_{\alpha_{\xi_1}}\left(\Lambda_{h,1}^{\mathrm{R}}-\left|\Lambda_{h,1}^{\mathrm{R}}\right|\right)+\frac{1}{2}\left(\Lambda_{h,1}^{\mathrm{L}}-\left|\Lambda_{h,1}^{\mathrm{L}}\right|\right)\mathsf{R}_{\beta_{\xi_1}}^{\mathrm{T}}\mathsf{H}_{\xi_1}^{\perp}\mathsf{R}_{\alpha_{\xi_1}}\right\}\boldsymbol{u}_h^{\mathrm{R}}\\
&-\frac{1}{2}\mathsf{H}^{-1}\left\{\frac{1}{2}\mathsf{R}_{\alpha_{\xi_2}}^{\mathrm{T}}\mathsf{H}_{\xi_2}^{\perp}\mathsf{R}_{\alpha_{\xi_2}}\left(\Lambda_{h,2}^{\mathrm{L}}+\left|\Lambda_{h,2}^{\mathrm{L}}\right|\right)+\frac{1}{2}\left(\Lambda_{h,2}^{\mathrm{L}}+\left|\Lambda_{h,2}^{\mathrm{L}}\right|\right)\mathsf{R}_{\alpha_{\xi_2}}^{\mathrm{T}}\mathsf{H}_{\xi_2}^{\perp}\mathsf{R}_{\alpha_{\xi_2}}\right\}\left(\boldsymbol{u}_h^{\mathrm{L}}-\tilde{\mathsf{I}}_{\xi_2}\boldsymbol{u}_{[3]}^{\mathrm{L}}\right)\\
&+\frac{1}{2}\mathsf{H}^{-1}\left\{\frac{1}{2}\mathsf{R}_{\beta_{\xi_2}}^{\mathrm{T}}\mathsf{H}_{\xi_2}^{\perp}\mathsf{R}_{\beta_{\xi_2}}\left(\Lambda_{h,2}^{\mathrm{L}}-\left|\Lambda_{h,2}^{\mathrm{L}}\right|\right)+\frac{1}{2}\left(\Lambda_{h,2}^{\mathrm{L}}-\left|\Lambda_{h,2}^{\mathrm{L}}\right|\right)\mathsf{R}_{\beta_{\xi_2}}^{\mathrm{T}}\mathsf{H}_{\xi_2}^{\perp}\mathsf{R}_{\beta_{\xi_2}}\right\}\left(\boldsymbol{u}_h^{\mathrm{L}}-\tilde{\mathsf{I}}_{\xi_2}\boldsymbol{u}_{[4]}^{\mathrm{L}}\right),
\end{aligned}
\tag{4}
$$

where $\tilde{\mathsf{I}}_{\xi_1}\coloneqq\mathbf{1}_{\xi_1}\otimes\mathsf{I}_{\xi_2}$, $\tilde{\mathsf{I}}_{\xi_2}\coloneqq\mathsf{I}_{\xi_1}\otimes\mathbf{1}_{\xi_2}$, and the volume metric terms in the left element are defined by

$$
\Lambda_{h,1}^{\mathrm{L}}\coloneqq\sum_{m=1}^{2}\mathrm{diag}\left(\mathcal{J}\frac{\partial \xi_1}{\partial x_m}\right)_h^{\mathrm{L}}\quad\text{and}\quad\Lambda_{h,2}^{\mathrm{L}}\coloneqq\sum_{m=1}^{2}\mathrm{diag}\left(\mathcal{J}\frac{\partial \xi_2}{\partial x_m}\right)_h^{\mathrm{L}}.
$$

For the global SBP-operator discretizations, the metrics are approximated using the global operators with one of the standard approaches. In two dimensions, this process is straightforward. In three dimensions, there are more possibilities. In Del Rey Fernández *et al.* [5], an example using the approach of Thomas and Lombard [17] is given.

3 High-Order Grids

Approaches for constructing grids based on B-spline and Lagrange mappings are considered to construct grids compatible with the orders of discretizations considered [2]. Descriptions of the different approaches may be found in [2]; however, some comments on the application of these approaches in the context of traditional finite-difference refinement and element-type refinement are presented here.

3.1 Traditional Refinement

For traditional SBP operators that have a repeated interior point operator, grid refinement can be performed by inserting additional grid nodes such that the resultant grid family is consistent. For CSBP operators, a consistent grid family can be constructed by starting with a fine grid and removing every second node in each block in each direction successively to construct a series of grids that are increasingly coarse. Alternatively, if one is interested in increasing the resolution of the series of grids by a factor other than two in each direction as the grid is refined, one can use the analytical B-spline mapping approach, which was the approach used by Hicken [9], for example, for some of his grid refinement studies.

In general, in the absence of a global analytical transformation, the use of the analytical B-spline mapping approach (or a similar approach) is also typically required to perform computations on a single grid as well as grid refinement studies with more general traditional SBP operators that do not necessarily have uniform nodal locations in computational space that include the boundary nodes [6, 13, 14]. This is because the coordinates in computational space will typically need to be modified from uniformly spaced nodes to reflect the nodal distribution of the SBP operators of interest, and the B-spline approach, for example, allows the nodal locations in computational space to be modified in a continuous way.

One caveat with the B-spline approach is that the intermediate parameters that arise from the least-squares fitting procedure are generally not uniformly spaced to ensure precise control of the grid in physical space in the context of grid deformation algorithms, where an additional intermediate mapping to uniform

computational coordinates is implied [9]. Note that it is possible that the use of uniformly spaced intermediate parameters could be sufficient to capture the initial grid if high-order grid generation is the priority instead of grid deformation. Regardless, when the intermediate parameters are nonuniformly spaced, to approximate the stretching of the intermediate parameters and the corresponding stretching of the grid within elements in physical space, the approach of Osusky [15] can be adopted whereby the stretching of the intermediate parameters is approximated via two-sided hyperbolic tangent stretching functions tuned through edge-spacing parameters. In this way, the nodal distribution in uniform computational coordinates can be set to the nodal distribution of the desired SBP operator and propagated through the intermediate mapping followed by the B-spline mapping to obtain the desired nodal locations in physical space.

3.2 Element-Type Refinement

For element-type refinement, it is possible to use either the Lagrange or the B-spline approach. For the Lagrange approach, the relationship between the number of interpolation nodes and the degree of the mapping is always $\overline{N} = p_g + 1$. For simplicity, and also due to the continuity requirement within elements, the same relationship (i.e., $\overline{N} = p_g + 1$) is chosen for the B-spline approach and the initial grid is always constructed such that, for each element, exactly the minimum number of nodes required to define a mapping of the desired degree is present. A consequence of this construction is that the least-squares fit for each element for the B-spline approach is exact to machine precision, with respect to reproducing the initial grid. Finally, because the B-spline mappings are constructed to have no interior knots for element-type grids, there is no need to introduce the modified B-spline basis functions used in [10] that permit spatially varying knots.

For the B-spline approach, like the traditional refinement case, two-sided hyperbolic tangent stretching functions can be used to capture some of the stretching of the initial grid within elements. For element-type grids, this might not be strictly necessary as one could argue that since the stretching of the initial grid is already being captured through element boundaries and the number of nodes in each element is small relative to the total number of elements, it is not as important as in the traditional case to capture the stretching within elements. Finally, note that traditional SBP operators can also be applied as element-type operators; however, purely element-type operators cannot be applied as traditional SBP operators due to the lack of repeated interior point operators.

4 Results

One- and two-dimensional problems are used to assess the performance of the different schemes: scalar linear boundary-value problems and subsonic channel flow over a Gaussian bump governed by the Euler equations.

4.1 One-Dimensional Scalar Linear Boundary-Value Problem

The purpose of this section is to highlight the main conclusion from [3], specifically that extrapolation operators of at least degree $2p$ are required to retain functional superconvergence in curvilinear coordinates when the metrics are approximated by the same SBP operator used in the overall discretization and the degree of the SBP operator used is lower than the degree of the geometry representation [3]. To appreciate this, consider discretizing a one-dimensional PDE with a source term $\mathcal{F}(x)$, where

$$\mathcal{F}(x) = \frac{\pi \mathrm{e}^x}{\mathrm{e}-1} \cos\left(\frac{\pi \mathrm{e}^x - \pi + \mathrm{e} - 1}{\mathrm{e}-1}\right),$$

such that the exact solution to the PDE is given by

$$\mathcal{U}(x) = \sin\left(\frac{\pi(\mathrm{e}^x - 1)}{\mathrm{e}-1} + 1\right).$$

A functional is used that includes both boundary and volume contributions. Furthermore, a grid function is used to stretch the nodal locations to obtain a variable metric Jacobian. Figure 2 provides the grid functions used. Table 1 gives the functional convergence rates when solving the one-dimensional PDE numerically. The

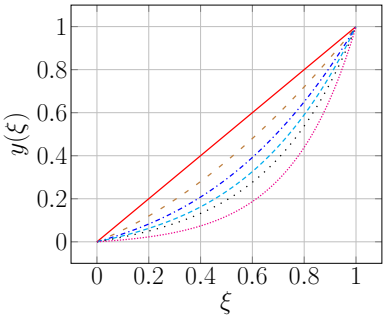

(a) Grid function plots.

Degree	Grid Function, $y(\xi)$	Line
1	ξ	———
2	$\frac{1}{2}\xi^2 + \frac{1}{2}\xi$	- - - -
3	$\frac{1}{3}\xi^3 + \frac{1}{3}\xi^2 + \frac{1}{3}\xi$	-·-·-·
4	$\frac{1}{4}\xi^4 + \frac{1}{4}\xi^3 + \frac{1}{4}\xi^2 + \frac{1}{4}\xi$	------
5	$\frac{1}{5}\xi^5 + \frac{1}{5}\xi^4 + \frac{1}{5}\xi^3 + \frac{1}{5}\xi^2 + \frac{1}{5}\xi$	.....
nonpolynomial	$(\exp(4\xi) - 1)/(\exp(4) - 1)$	.....

(b) Grid function expressions.

Figure 2: Grid functions for variable metric Jacobian.

Table 1: Representative functional error convergence rates for different grid functions for the one-dimensional scalar linear boundary-value problem. Rates less than $\tau + 1$ are boxed.

Operator	ξ	$\frac{1}{2}\xi^2 + \frac{1}{2}\xi$	$\frac{1}{3}\xi^3 + \frac{1}{3}\xi^2 + \frac{1}{3}\xi$	$\frac{1}{4}\xi^4 + \frac{1}{4}\xi^3 + \frac{1}{4}\xi^2 + \frac{1}{4}\xi$	$\frac{1}{5}\xi^5 + \frac{1}{5}\xi^4 + \frac{1}{5}\xi^3 + \frac{1}{5}\xi^2 + \frac{1}{5}\xi$	$(\exp(4\xi) - 1)/(\exp(4) - 1)$
	MFD1	MFD2	MFD3	MFD4	MFD5	MFNP
LGLp1	2.00	2.01	1.98	1.98	1.99	1.99
LGLp2	4.00	4.20	4.00	4.00	4.00	4.00
LGLp3	6.00	5.98	6.05	5.80	5.66	6.89
LGLp4	8.40	8.64	8.01	7.92	7.83	7.84
LGp1	4.01	2.00	1.99	1.97	1.97	1.95
LGp2	6.00	5.95	2.00	2.00	2.00	2.00
LGp3	8.69	7.96	8.23	3.96	4.02	4.01
LGp4	9.48	9.38	10.39	10.75	4.00	4.01

best-case convergence rates with LGL and LG operators are $2p$ and $2p+2$, respectively. For all LGL operators, approximately $2p$ convergence is obtained. However, the LG operators only obtain $2p+2$ convergence when the degree of the grid function is less than or equal to the SBP operator used to approximate the metrics.

4.2 Two-Dimensional Scalar Linear Boundary-Value Problem

In this section, conclusions from [2] are highlighted that involve the extension to a two-dimensional scalar linear boundary-value problem. Specifically, a steady two-dimensional scalar linear boundary-value problem is considered, and the source terms are chosen such that the exact primal and dual solutions are defined by

$$\mathcal{U}_{\text{exact}}(x, y) \coloneqq \sin(2\pi x) + \sin(2\pi y) \text{ and}$$
$$\psi_{\text{exact}}(x, y) \coloneqq \sin(2\pi x) + \frac{\exp(y) - 1}{\exp(1) - 1},$$

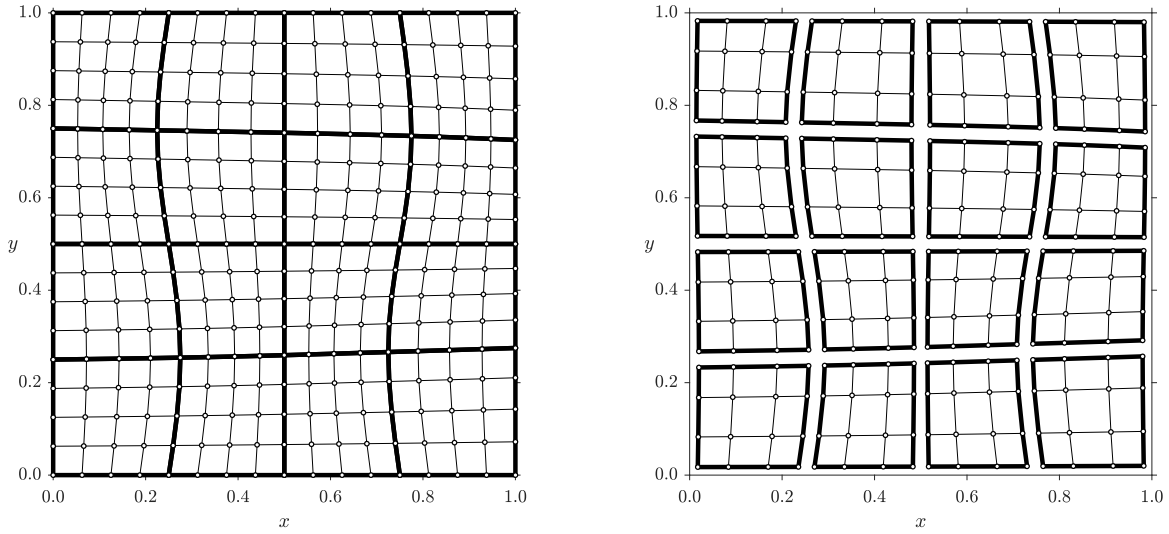

(a) Initial grid with 5×5 uniform nodes in each element. (b) Final grid with 4×4 $p = 3$ LG nodes in each element.

Figure 3: Example high-order grid for Ω with $K = 16$ nonoverlapping elements. A degree $p_g = 4$ element-local Lagrange mapping is defined on each element of the initial grid based on the uniform nodes. The element-local mappings are subsequently used to repopulate the elements with the $p = 3$ LG nodes to generate the final grid.

Table 2: Test case matrix for the two-dimensional scalar linear boundary-value problem.

Type of discretization	**Form of equation**	**Metrics**	**Mapping**	p_g
Mortar-element	Div/Skew	Baseline	Lagrange	p
Mortar-element	Div/Skew	Baseline	Lagrange	$p+1$
Mortar-element	Div/Skew	Modified	Lagrange	$p+1$
Global SBP-operator	Div/Skew	Global	Lagrange	p
Global SBP-operator	Div/Skew	Global	Lagrange	$p+1$

respectively. The grid is constructed via an analytical transformation followed by a Lagrange mapping approach, as shown in Figure 3. The functional of interest includes both volume and boundary contributions. More details are provided in [2].

The schemes considered are summarized in Table 2. Although this specific problem does not require the use of a degree $p+1$ mapping, when solving more complex nonlinear problems the use of higher degree mappings can be beneficial (see, for example, [1]), which motivates the study of the use of higher degree mappings in the present linear context. The accuracy of each scheme considered is evaluated in terms of truncation, solution, and functional error, for both the primal and dual discretizations. The truncation error should be $\mathcal{O}(h^p)$ to confirm that the primal and dual discretizations are consistent and dual consistent, respectively. The solution error should be at least $\mathcal{O}(h^p)$ with $\mathcal{O}(h^{p+1})$ often being observed in the literature. The functional error is considered to be superconvergent if it is at least $\mathcal{O}(h^{2p})$ and anything less is considered suboptimal. Finally, the truncation error and functional error are assessed using the infinity norm and the solution error is assessed using the global H-norm.

In terms of accuracy, it was found that the mortar-element divergence and skew-symmetric discretizations give similar results, likewise for the global SBP-operator divergence and skew-symmetric discretizations. The functional superconvergence results for the mortar-element schemes are summarized in Table 3. When using degree p Lagrange mappings in each element, close to optimal truncation and solution error convergence rates are observed, along with functional superconvergence for both the LGL and LG families of operators. The preceding statement applies to both the mortar-element and global SBP-operator approaches. When using degree $p+1$ Lagrange mappings, the functional convergence rates with the LG operators are significantly

Table 3: Mortar-element approach superconvergence matrix (metrics: baseline or modified, degree of mapping: p or $p+1$) for the two-dimensional scalar linear boundary-value problem.

Operator	**Baseline,** p	**Baseline,** $p+1$	**Modified,** $p+1$
LGL	✔	✔	✔
LG	✔	✘	✔

Table 4: Global SBP-operator approach superconvergence matrix (metrics: global, degree of mapping: p or $p+1$) for the two-dimensional scalar linear boundary-value problem.

Operator	**Global,** p	**Global,** $p+1$
LGL	✔	✔
LG	✔	✘

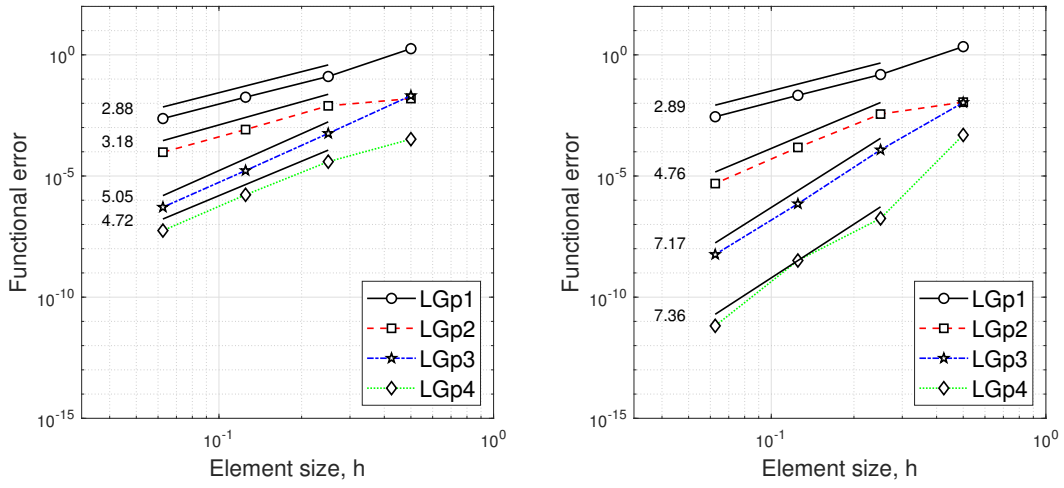

(a) LG, $p+1$, global.

(b) LG, $p+1$, modified.

Figure 4: Comparison of skew-symmetric discretizations for the two-dimensional scalar linear boundary-value problem. Global SBP-operator approach on left, mortar-element approach on right. Each subcaption gives the operator family, degree of mapping, and approach for the metrics, respectively.

reduced with the baseline approach for the metrics relative to the LGL operators and relative to the LG operators with the degree p mappings, due to the degree p accuracy of the LG extrapolation operators. Note that because the dual truncation error still converges at a rate close to p, this indicates that this loss of functional superconvergence is not due to a lack of dual consistency. With respect to the present accuracy measures being studied, the main benefit of the modified approach for the metrics is the retention of functional superconvergence with LG operators when using degree $p+1$ mappings.

The functional superconvergence results for the global SBP-operator schemes are summarized in Table 4. Superconvergence is obtained with degree p mappings. However, superconvergence is only obtained with the LGL operators with degree $p+1$ mappings (a similar trend is observed when using exact mappings), despite the dual truncation error converging close to order p. Therefore, functional accuracy could be considered as a criterion for potentially preferring the mortar-element approach over the global SBP-operator approach. To emphasize this point, Figure 4 compares the functional error convergence for global SBP-operator and mortar-element discretizations with degree $p+1$ mappings. Only the mortar-element discretizations obtain superconvergence for all operators.

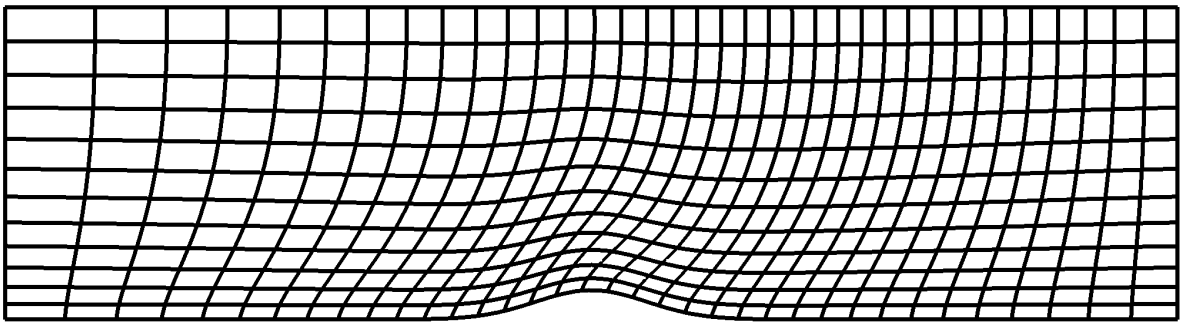

(a) Second coarsest grid with $p = 3$ LGL nodes in each element. Only the element boundaries are shown.

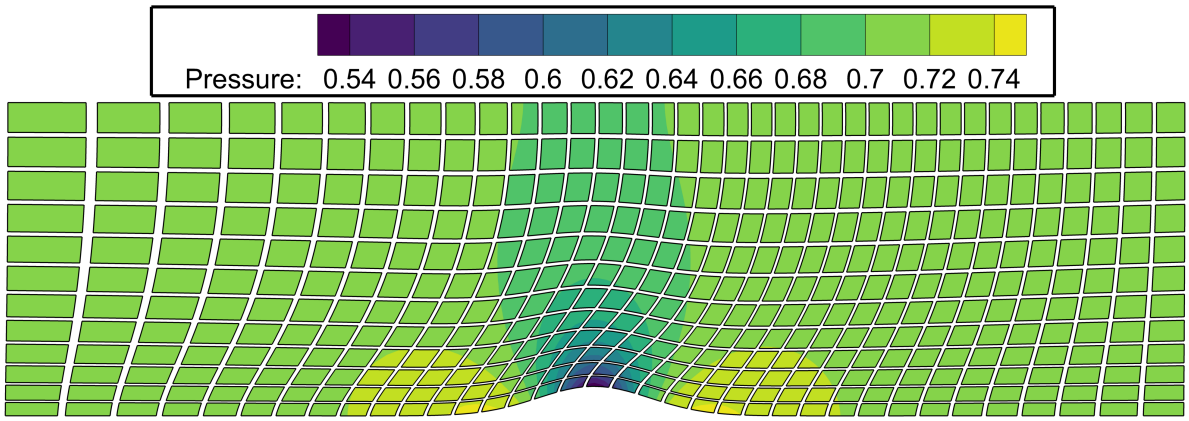

(b) Numerical solution on second coarsest grid with $p = 3$ LG operators. Pressure contours are shown.

Figure 5: Grid and numerical solution for the subsonic channel flow over a Gaussian bump problem governed by the Euler equations.

4.3 Two-Dimensional Subsonic Channel Flow Over a Gaussian Bump

In this section, the extension to the Euler equations is discussed in the context of a two-dimensional subsonic channel flow over a Gaussian bump problem. Figure 5 shows a grid and numerical solution for this problem. The functional of interest is a weighted lift over the surface of the bump. Only the divergence form of the Euler equations is considered, as it is expected that the skew-symmetric form will give similar results in terms of accuracy based on the results from the two-dimensional scalar problem. Furthermore, the mortar-element approach is used due to its ability to obtain functional superconvergence with degree $p+1$ mappings via the modified metrics, in contrast to the global SBP-operator approach.

Table 5 summarizes the functional convergence results for the subsonic channel flow over a Gaussian bump problem. In contrast to the scalar problem results, the degree p mappings do not lead to superconvergence in general due to the insufficient accuracy of the wall normal in the flow tangency boundary condition [2]. Similar to the scalar problem, superconvergence with degree $p+1$ mappings is obtained for LGL and not LG operators with baseline metrics. However, superconvergence with degree $p+1$ mappings for LG operators is recovered with modified metrics.

5 Conclusions

High-order tensor-product generalized SBP discretizations have been investigated and conditions for obtaining accurate functionals for CFD problems of increasing practical complexity have been delineated. Results in one and two dimensions involving linear and nonlinear problems have been discussed. Future work will

Table 5: Mortar-element approach superconvergence matrix (metrics: baseline or modified, degree of mapping: p or $p+1$) for the subsonic channel flow over a Gaussian bump problem.

Operator	**Baseline,** p	**Baseline,** $p+1$	**Modified,** $p+1$
LGL	✘ (wall normal)	✔	✔
LG	✘ (wall normal)	✘	✔

focus on investigating analogous conditions for obtaining functional superconvergence from more complex problems involving large eddy simulations and the Reynolds-averaged Navier-Stokes equations.

References

[1] Bassi, F., Rebay, S.: High-order accurate discontinuous finite element solution of the 2D Euler equations. Journal of Computational Physics **138**, 251–285 (1997)

[2] Craig Penner, D.A., Zingg, D.W.: Accurate high-order tensor-product generalized summation-by-parts discretizations of hyperbolic conservation laws: general curved domains and functional superconvergence. Submitted to Journal of Scientific Computing

[3] Craig Penner, D.A., Zingg, D.W.: Superconvergent functional estimates from tensor-product generalized summation-by-parts discretizations in curvilinear coordinates. Journal of Scientific Computing **82**(41) (2020)

[4] Crean, J., Hicken, J.E., Del Rey Fernández, D.C., Zingg, D.W., Carpenter, M.H.: Entropy-stable summation-by-parts discretization of the Euler equations on general curved elements. Journal of Computational Physics **356**, 410–438 (2018)

[5] Del Rey Fernández, D.C., Boom, P.D., Carpenter, M.H., Zingg, D.W.: Extension of tensor-product generalized and dense-norm summation-by-parts operators to curvilinear coordinates. Journal of Scientific Computing **80**(3), 1957–1996 (2019)

[6] Del Rey Fernández, D.C., Boom, P.D., Zingg, D.W.: A generalized framework for nodal first derivative summation-by-parts operators. Journal of Computational Physics **266**, 214–239 (2014)

[7] Del Rey Fernández, D.C., Hicken, J.E., Zingg, D.W.: Simultaneous approximation terms for multi-dimensional summation-by-parts operators. Journal of Scientific Computing **75**(1), 83–110 (2018)

[8] Hartmann, R.: Adjoint consistency analysis of discontinuous Galerkin discretizations. SIAM Journal on Numerical Analysis **45**(6), 2671–2696 (2007)

[9] Hicken, J.E.: Efficient algorithms for future aircraft design: Contributions to aerodynamic shape optimization. Ph.D. thesis, University of Toronto (2009)

[10] Hicken, J.E., Zingg, D.W.: Aerodynamic optimization algorithm with integrated geometry parameterization and mesh movement. AIAA Journal **48**(2), 400–413 (2010)

[11] Hicken, J.E., Zingg, D.W.: Superconvergent functional estimates from summation-by-parts finite-difference discretizations. SIAM Journal on Scientific Computing **33**(2), 893–922 (2011)

[12] Hicken, J.E., Zingg, D.W.: Dual consistency and functional accuracy: a finite-difference perspective. Journal of Computational Physics **256**, 161–182 (2014)

[13] Mattsson, K., Almquist, M., Carpenter, M.H.: Optimal diagonal-norm SBP operators. Journal of Computational Physics **264**, 91–111 (2014)

[14] Mattsson, K., Almquist, M., van der Weide, E.: Boundary optimized diagonal-norm SBP operators. Journal of Computational Physics **374**, 1261–1266 (2018)

[15] Osusky, L.M.: A numerical methodology for aerodynamic shape optimization in turbulent flow enabling large geometric variation. Ph.D. thesis, University of Toronto (2014)

[16] Pulliam, T.H., Zingg, D.W.: Fundamental Algorithms in Computational Fluid Dynamics. Scientific Computation. Springer International Publishing (2014)

[17] Thomas, P.D., Lombard, C.K.: Geometric conservation law and its application to flow computations on moving grids. AIAA Journal **17**(10), 1030–1037 (1979)

[18] Worku, Z.A., Zingg, D.W.: Simultaneous approximation terms and functional accuracy for diffusion

problems discretized with multidimensional summation-by-parts operators. Journal of Computational Physics **445** (2021)

[19] Yan, J., Crean, J., Hicken, J.E.: Interior penalties for summation-by-parts discretizations of linear second-order differential equations. Journal of Scientific Computing **75**(3), 1385–1414 (2018)